Mon. Not. R. Astron. Soc. **000**, 000–000 (0000) Printed 27 December 2012 (MN LaTeX style file v2.2)

arXiv:1212.6171v1 [astro-ph.CO] 26 Dec 2012

A multi-wavelength study of nuclear activity and environment of a low power radio galaxy CTD 86

M. B. Pandge [1]⋆, G. C. Dewangan[2], K. P. Singh[3], M. K. Patil[1]

[1] *Swami Ramanand Teerth Marathwada University Nanded 431606, India*

[2] *Inter-University Centre for Astronomy and Astrophysics, Post Bag 4, Ganeshkhind, Pune 411007, India*

[3] *Tata Institute of Fundamental Research, Mumbai 400005, India.*

27 December 2012

ABSTRACT

We present multiwavelength X-ray, optical and radio study of the Fanaroff & Riley class I radio galaxy CTD 86 based on *XMM-Newton*, *ROSAT*, Sloan Digital Sky Survey (SDSS), Vainu Bappu Telescope (VBT) observations and the Faint Images of the Radio Sky at Twenty centimeters (FIRST) survey. X-ray emission from CTD 86 originates from two components - diffuse thermal emission from hot gas ($kT \sim 0.9$ keV, $n_e \sim 10^{-3}$ cm^{-3}, $L_X \sim 5\times10^{42}$ ergs s^{-1} and size $\sim$ 186 kpc), and a central point source representing the active nucleus. The hot gaseous environment of CTD 86 is similar to those found in galaxy groups or bright early-type galaxies. We found no clear signature of radio-lobes interacting with the diffuse hot gas. X-ray emission from the active nucleus is well described by an intrinsically absorbed ($N_H \sim 5.9\times10^{22}$ cm^{-2}) power law ($\Gamma \sim 1.5$) with a $2-10$ keV luminosity $L_X \sim 2.1\times10^{42}$ ergs s^{-1}. CTD 86 has a weak optical emission line spectrum typical of type 2 active galactic nuclei (AGN). The nuclear X-ray, Hα, and radio luminosities of CTD 86 are lower than those of luminous AGN. We have measured the stellar velocity dispersion, $\sigma = 182\pm8$ km s^{-1}, of CTD 86 and estimated the mass of central black hole, $M_{BH} \sim 9\times10^7$ M$\odot$, accreting at a rate of $\dot{m} = L_{bol}/L_{Edd} \sim 4\times10^{-3}$. The low accretion rate and high $L_X/L_{[O\ III]}$ ratio suggest that the central engine of CTD 86 consists of a truncated accretion disk lacking a strong ionizing UV radiation and an inner hot flow producing the X-ray emission. The truncated disk is likely inclined with $i \sim 40-50$ deg such that our line of sight passes through the outer regions of a putative torus and thus resulting in high X-ray absorption. We also report two additional bright X-ray point sources, SDSS J142452.11+263715.1 and SDSS J142443.78+263616.2, near CTD 86 for the first time. SDSS J142452.11+263715.1 shows broad optical emission lines with $z = 0.3761$ and unabsorbed $0.3 - 10$ keV X-ray luminosity $L_X \sim 8 \times 10^{43}$ ergs s^{-1}, making this object a type 1 AGN. SDSS J142452.11+263715.1 hosts an AGN as suggested by its X-ray to optical flux ratio. SDSS J142443.78+263616.2 is likely a galaxy that hosts an AGN.

Key words: galaxies: active; galaxies: elliptical and lenticular, cD; galaxies: nuclei; galaxies: individual: CTD 86; X-rays: galaxies; X-rays: individual: RX J1424.7+2636

1 INTRODUCTION

The optical and X-ray luminosity functions of active galactic nuclei (AGN) are not complete at the faint end of corresponding luminosities. Therefore, in order to understand the nature and evolution of AGN, it is important to study low luminosity AGN in optical and X-ray bands. Both radio-quiet as well as radio-loud active galaxies are expected to exist at low optical and X-ray luminosities. The nearby low-power radio galaxies are good candidates to study the mild nuclear activity in galaxies. Super massive black holes, accretion discs, broad line regions (BLRs), narrow line regions (NLRs) etc., all are thought to be associated with low luminosity radio galaxies (LLRGs). Therefore, study of LLRGs may enable us to estimate some of the basic parameters, e. g., black hole masses, accretion rate, velocities of (BLRs),(NLRs) etc., governing the overall appearance of these galaxies. Study of LLRGs have also been stimulated by the fact that they play a fundamental role in the unification schemes of radio galaxies as they are thought to be the parent population of BL Lac objects. The LLRGs are members of Fanaroff-Riley Type 1 (FR-I) (Fanaroff & Riley 1974) class, where one finds a variety of sources in terms of power and radio morphology. Apart from having radio power $\leqslant 5 \times 10^{25}$ W Hz^{-1} at a frequency of 1.4 GHz, FR I sources have only one feature in common: hot spots at the outer edge of lobes are never seen. Naked radio jets occur preferably at the very low end of radio power ($< 10^{23}$WHz^{-1}), while at the upper end ($\sim 10^{25}$ W Hz^{-1}) , one sided jets and hot spots in the middle of the lobes are seen. In the intermediate power range prominent twin-jets symmetrical at large scales but asymmetrical close to the nucleus, are seen. The asymmetry appears to be more pronounced in case of stronger sources (Parma et al. 1999). The radio emission is thought to arise from the synchrotron radiation mechanism and is a manifestation of nuclear activity. The nuclear activity is also inferred from other independent means such as optical and X-ray emission. In optical spectra of radio galaxies, nuclear activity results in a wide range of ionization (from low stages, such as [O I], [S II] lines, to high stages through [Ne V], [Fe VII] lines), broad and narrow permitted as well as forbidden lines are evident. The broad-line radio galaxies, equivalent to Seyfert 1 galaxies, show broad H I, He I, and He II emission lines but narrower forbidden lines. The narrow-line radio galaxies, similar in optical emission line spectrum to Seyfert 2 galaxies, show narrow permitted and forbidden lines. At X-ray wavelengths, nuclear activity is identified by a strong power-law continuum, rapid variability and high luminosity. X-ray evidence for the existence of low level nuclear activity in many galaxies has yet to be confirmed. There are X-ray detections of mild nuclear activity in some galaxies. Bregman et al. (1995) have reported a point-like soft X-ray emission from the S0 galaxy NGC 4203. Iyomoto et al. (1998) have found hard X-ray emission from a point-like source at the nucleus of NGC 4203, and have fitted a single power-law model to the hard X-ray spectrum of NGC 4203. Based on *Chandra* observations of 62 galaxies from the Spitzer Infrared Nearby Galaxy Survey, Grier et al. (2011) detected 37 nuclear X-ray sources, many of which are likely to be AGN.

---

* E-mail: mbpandge@gmail.com

The massive elliptical host galaxies, many of which contain radio-loud AGN, are associated with large amount of hot gas with temperatures of $10^6 - 10^8$ K (Sarazin 1986; Mulchaey 2000; Mathews & Brighenti 2003; Hardcastle 2005). The gas is heated in the deep gravitation potential wells of the massive elliptical galaxies or the associated groups or clusters of galaxies. It is now well known that the radio lobes and jets of the radio-loud AGN interact with the environment and can efficiently heat the surrounding medium and thus prevent the accumulation of large amounts of cool gas in the central regions (Hardcastle 2005, and references therein). However, it is not known clearly if the LLRGs are powerful enough to affect their surroundings.

It is also not clear if all FR I galaxies have central X-ray core similar to that of radio-quiet AGNs such as Seyfert galaxies. Donato et al. (2004) found central compact X-ray cores in 13 out of 25 FR-I radio galaxies from the 3CRR (Spinrad et al. 1985) and B2 (Colla et al. 1975; Fanti et al. 1978) catalogs. Canosa et al. (1999) and Donato et al. (2004) have found X-ray core and radio luminosities in their study of radio galaxies suggesting that at least some of the X-ray emission is related to the nuclear jet. The point-like nuclear X-ray luminosity of the low power radio galaxies range from below $3 \times 10^{40}\mathrm{erg\,s^{-1}}$to $5.4{\times}10^{44}$ $\mathrm{erg\,s^{-1}}$(Canosa et al. 1999). Donato et al. (2004) found very small Eddington ratios, $L_{bol}/L_{Edd} \sim 10^{-3} - 10^{-8}$ and no strong X-ray absorption and have suggested that FR-I galaxies generally lack a standard torus. However, it is difficult to see strong X-ray absorption if the bulk of the X-ray emission is arising from a jet. Since the Eddington ratios of FR-I galaxies are very small compared to that for Seyfert 1 and quasars, it is possible that central engine of FR I galaxies is different from that of other AGN with high Eddington ratios. Multiwavelength study of central compact core of FR-I galaxies is required to make any progress on our understanding of their central engines.

Here, we present a multiwavelength study of an FR-I radio galaxy CTD 86 (CalTech list D of radio sources), also known as (B2 1422+26). CTD 86 is a low-power radio galaxy (Parma et al. 1987; Canosa et al. 1999) with radio power $1.9{\times}10^{24}WHz^{-1}$ at 1.4 GHz, photometric B band magnitude of 15.62 and is located at a distance of about 161 Mpc (H_0 =73 km s^{-1} Mpc^{-1}, z=0.037). CTD 86 is an elliptical (E2-type) radio galaxy (Merkelijn 1968). It has been detected in the field of a poor galaxy cluster AWM 3 (Beers et al. 1984) with ∼44 galaxies in it. However, CTD 86 is unlikely to be the member of this cluster as its recessional velocity ($cz = 10171$ km s^{-1}) is much higher than that of the kinematically central galaxy NGC 5629 ($cz = 4495$ km s^{-1}) of the poor cluster AWM 3. The global parameters of CTD 86 are summarized in Table 1. The radio source associated with CTD 86 shows a symmetric double lobed structure with hot spots approximately at the middle of the lobes. These lobes are found to extend up to about 75 kpc from the optical center of the galaxy. At the outer edges of the lobes, symmetrical ring like structures are also evident. The radio jets of CTD 86 are not well defined (Becker et al. 1994). The FIRST (Faint Images of the Radio Sky at Twenty Centimeters) survey (Becker et al. 1994)) image of CTD 86 with an average resolution of 5 arcsec exhibits a weak one-sided jet like structure. In this paper, we present X-ray imaging and spectroscopy based on *XMM-Newton* and *ROSAT* observations, and optical imaging and spectroscopy based on observations from Vainu Bappu Telescope (VBT) & Sloan Digital Sky Survey (SDSS), respectively. The structure of this paper is as follows. Section 2 describes the multiwavelength data on CTD 86. Section 3 deals with reduction and analysis of the multiwavelength data. Results of X-ray and optical analysis are discussed in section 4 and 5 followed by conclusions in Section 6.

All distance dependent parameters have been computed assuming luminosity distance to

Table 1. Global parameters of CTD 86

α (J2000); δ (J2000)	14:24:40.5; +26:37:31
Morphological type^1	E2
Magnitude (B)	15.62
Size	$0'.96\times0'.66$
Distance (Mpc)	161
z	0.037152
Radio core flux density^2 (f_{5GHz})	25mJy

[1] Merkelijn (1968); [2] Giovannini et al. (1991)

CTD 86 of 161 Mpc that gives a scale of $1''$= 744 pc. The cosmological parameters assumed are $\Omega_m = 0.27$, $\Omega_\Lambda = 0.73$ and H_0 =73 km s^{-1} Mpc^{-1}.

2 MULTIWAVELENGTH DATA

We have used ground-based optical and radio observations and space-based X-ray observations of CTD 86. Optical observations under photometric conditions were carried out at the 234 *cm* Vainu Bappu Telescope (VBT), Kavalur (India). The B band images of CTD 86, along with necessary calibration frames, were acquired on the night of 1999 March 13 at the prime focus of the VBT equipped with TEK 1024 × 1024 CCD chip. The B band exposure time was 600 s. The pixel size of 24 µm square per pixel of the CCD chip gives a scale of $0.61''$ per pixel and a total field of $10.41' \times 10.41'$. The observation were carried out under photometric conditions with seeing ($FWHM$) about $2.6''$. The standard star field in the "dipper asterism" region of the open cluster M 67 was observed for photometric calibration. Optical images and spectra available in the archive of the Sloan Digital Sky Survey[1] were also used for the present study.

CTD 86 was observed in soft X-rays with the *ROSAT* High Resolution Image (HRI) (Truemper 1982; Pfeffermann et al. 1987) on 1995 January 23-24 and on 1996 January 15-19. The observations were essentially on-axis, the mean off-set angle from the center of the field of view of HRI in both observations was $\simeq 1.5'$. ROSAT X-ray data of both the observations were obtained from the public archives maintained at the High Energy Astrophysics Science Archive Research Center (HEASARC) in USA. The data are referred by the sequence numbers rh701830n00 and rh701830a01, and the effective exposure times were 13.1 ks and 18.2 ks in the first and second observation, respectively.

CTD 86 was also observed with the *XMM-Newton* twice on 2010 June 21 (obsid: 0652720101 hereafter Ob.I) and an 2010 August 02 (obsid: 0652720201 hereafter Ob.II). The effective

---

[1] SDSS is the Data base http://www.sdss.org

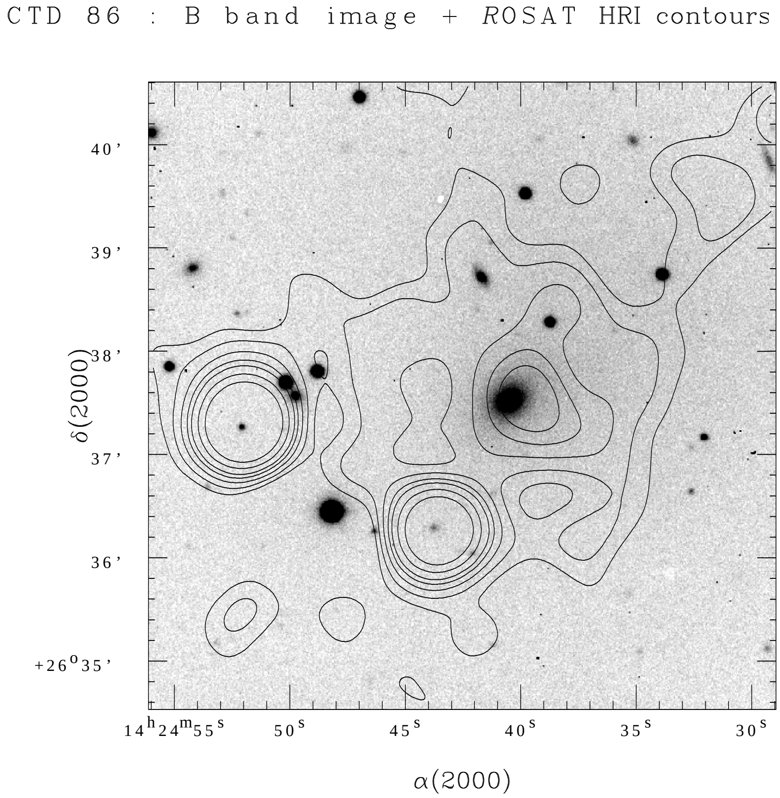
CTD 86 : B band image + *ROSAT* HRI contours

Figure 1. *B* band optical image of CTD 86 overlaid on which are the contours of *ROSAT* HRI image. The contours are drawn at 2σ, 3σ, 5σ, 7σ, 9σ, 13σ, and 19σ above background level (0.0082 ± 0.0007 counts s^{-1}). Extended X-ray emission associated with CTD 86 is clearly seen. Two bright point X-ray sources seen here are listed in Table 4.

Table 2. ROSAT data analysis of two point sources close to CTD 86

Source Name	α(J2000)	δ(J2000)	SDSS u magnitude	1995 Jan.23 count rate[a]	f_x^b	1996 Jan. 15 count rate[a]	f_x^b
SDSS J142452.11+263715.1	14:24:52.1	+26:37:30	19.02	69±9	3.28	73±8	3.4
SDSS J142443.78+263616.2	14:24:43.8	+26:36:18	20.30	6.1±6.6	0.29	89±8	4.2

[a] Count rate is in unit of 10^{-4} counts s^{-1}.
[b] Unabsorbed X-ray flux in the $0.1-2.0$ keV band and in the units of 10^{-13} erg cm^{-2} s^{-1}.

exposure times for the two observation were 33.9 ks and 32.4 ks, respectively. In both the observations, the three EPIC cameras were operated in the full frame mode using the "Thin" filter for the EPIC-pn Strüder et al. (2001) and "medium" filter for the two MOS cameras (Turner et al. (2001)). The data were obtained from the HEASARC archives. We have used both the observations to study the X-ray properties of CTD 86.

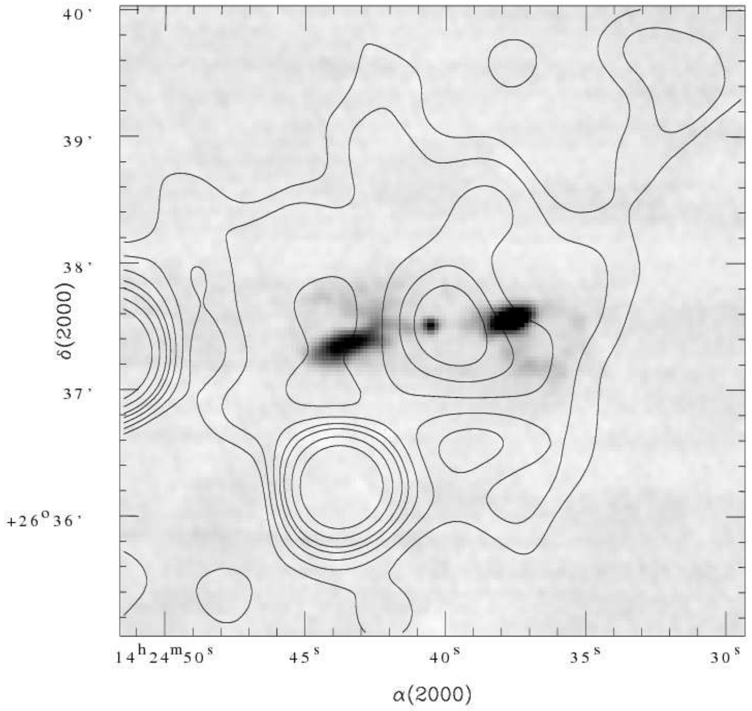

Figure 2. The radio image of CTD 86 at 20-cm taken from the FIRST survey, overlaid on which are the contours of ROSAT HRI image. The X-ray contours are drawn at 2σ, 3σ, 5σ, 7σ, 9σ,13σ and 19σ above the background level (0.0082± 0.0007 countss^{-1}).

3 X-RAY IMAGING & SPECTROSCOPY

3.1 The *ROSAT* Data

ROSAT soft X-ray data were analysed using the PROS[2] software package. HRI images were extracted from both the observations mentioned above. These images were combined to increase the signal-to-noise ratio. The combined X-ray images were smoothed by convolving with a Gaussian of width 15″. The contours of *ROSAT* HRI X-ray surface brightness overlaid on the B band image of CTD 86 are shown in Figure 1. We also show the contours of *ROSAT* HRI X-ray surface brightness overlaid onto the FIRST radio image of CTD 86 in Figure 2. Extended X-ray emission centered on CTD 86 is seen in both the observations. The extended emission is symmetric. Two bright point like sources are observed to dominate the X-ray emission in the east and south. The contributions of these two sources are required to be subtracted from the over all emission to obtain an accurate count rate that can be attributed to CTD 86. For this purpose, we generated radial profiles of the two sources using the raw (unsmoothed) data and confirmed that these are indeed point sources. The procedure followed is as follows: Two images representing the on-axis point response of the ROSAT HRI at the positions of the point sources were created using the PROS task 'rosprf'. Each image was smoothed in the same manner as described above and then scaled to match the peak counts of the point source at the same position in the HRI image. Thus we created *ROSAT* HRI model images of the two point sources, and subtracted them from the smoothed HRI image to exclude the contribution of the point sources. The extended X-ray emission associated with CTD 86 was derived thus. This was further checked by looking at the model profile made from the raw data and comparing it with the point response function of HRI. The linear size of the extended X-ray emission associated with CTD 86 is about $\sim 4'$($\sim$180 kpc). A slight radial asymmetry is seen in the extended X-ray emission as was also pointed by Canosa et al. (1999) and is not due to the *ROSAT* aspect correction problem. Total counts for CTD 86 were extracted from the smoothed, point source removed X-ray image using a circle of radius $100''$ and centered at the extended emission. Background counts were obtained from $100''$ wide annuls outside the $125''$ radius from the center, and subtracted from the total source counts after scaling the background to the same number of pixels as in the source. The total counts thus derived are 250 ± 38 , which agree well with the value of 254 ± 40 derived by Canosa et al. (1999). The corresponding count rate of 0.0080 ± 0.0025 counts s^{-1} was converted to X-ray flux in the *ROSAT* HRI band of $(0.1-2.4)$ keV assuming Raymond-Smith (RS) plasma model. This model is appropriate for hot gas (kT$\simeq$ 1 keV) found in the X-ray bright elliptical galaxies and also for hot gas (kT $\simeq$ 3 keV) present in groups of galaxies. The unabsorbed X-ray flux (0.1$-$ 2.4 keV) of the extended emission associated with CTD 86 was found to be $3.5\times10^{-13} erg\ s^{-1} cm^{-2}$ by using the RS model (kT = 3 keV) modified by Galactic absorption along the line of sight to the source. The Galactic absorption was kept fixed at the 21-cm value of $1.6 \times 10^{20} cm^{-2}$. The corresponding X-ray luminosity associated with CTD 86 is $9.5\times10^{41} erg\ s^{-1}$. If, we assume a value of 1 keV for kT of the RS plasma, then the X-ray flux and luminosity of the extended emission associated with CTD 86 are found to be $2.7 \times 10^{-13} erg\ s^{-1} cm^{-2}$ and $7.2\times10^{41} erg\ s^{-1}$, respectively.

---

[2] The PROS Software package provided by the *ROSAT* Science Data Center at Smithsonin Astrophysical Observatory

Two bright point X-ray sources detected close to CTD 86 are also apparent in the B band optical image shown in Figure 1 (see also Figure 4). The X-ray count rates from these sources were estimated separately for each observation. Total counts from the two sources were extracted using circles of radius $30''$ centered on the peak of the sources. Background counts for each source were derived from a circle of radius $60''$ in the source free regions close ($< 3'$, and $> 1'$) to point sources. Count rates were then converted into the X-ray flux using PROS task 'hxflux' in the *ROSAT* HRI band (0.1−2.0) keV. Since we suspect these sources to be distant AGN, we assumed a power-law model with photon index, (Γ) of 2.0 modified by the Galactic absorption for these sources. The Galactic absorption was kept fixed at the 21-cm value along the line of sight to the source. Table 2 lists the X-ray count rate, X-ray flux, SDSS identifier, position, and 'u' band magnitude for both the point sources. Flux of the source SDSS J142452.11+263715.1, listed in Table 2, is constant within errors in the two observations. This object appears to be point like in the SDSS R band optical image. The second object, SDSS J142443.78+263616.2, listed in Table 2, exhibits variability, with its X-ray flux varying by almost an order of magnitude in one year. This object appears as an extended object in SDSS R band optical image, and therefore most likely to be a galaxy. In order to find the nature of the two objects listed in Table 2, we have calculated the ratio of X-ray flux in the energy band (0.3−3.5) keV to the optical flux in the V band $\log(\frac{f_X}{f_V})$ following Maccacaro et al. (1988). The X-ray flux for each object was estimated in the same way as discussed above in the energy band (0.3−3.5) keV using the second observation only. Optical V band magnitudes were taken from USNO Catalogue. We found $\log(\frac{f_X}{f_V})$ to be 0.26 and 0.27 for the first and second object, respectively. These values indicate that both the objects are AGN (see Maccacaro et al. (1988)). The high variability of the second object indicates a transient source or an AGN.

3.2 The *XMM-Newton* data

3.2.1 X-ray images and Radial profile

The observation data files (ODF) for CTD 86 obtained from the *XMM-Newton* observatory of CTD 86 were processed using the Science Analysis Software (SAS) version 11. Examination of the background rate above 10 keV showed that the observations were partly affected by the flaring particle background. The periods of flaring particle background were identified and removed based on the count rate threshold. Time intervals with a count rate greater than 0.6 counts s^{-1} for the EPIC-pn and 0.175 counts s^{-1} for MOS1 and MOS2 cameras were identified as flares and were excluded from rest of the analysis. Only events corresponding to patterns 0–4 for the EPIC-pn and 0–12 for the MOS cameras were retained for further

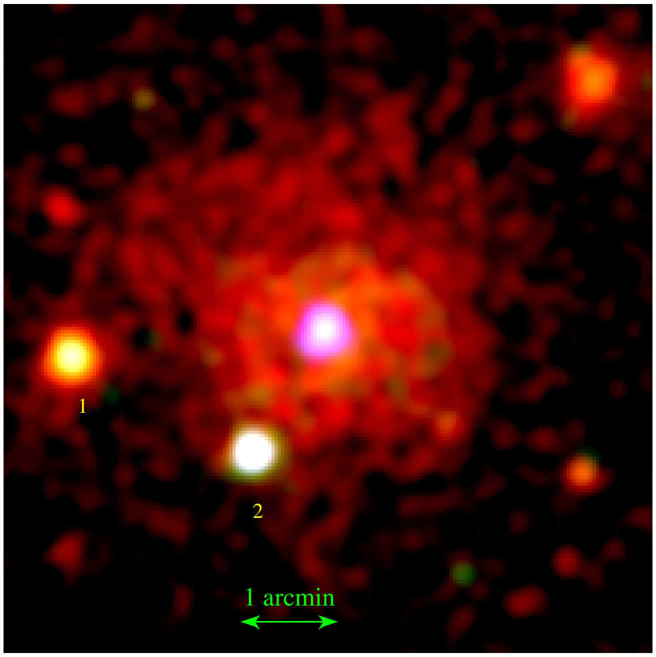

Figure 3. *XMM-Newton* tri-color image of CTD 86 and its environment. The soft ($0.3-1$ keV) band is shown in red, the intermediate ($1-2$ keV) band in green and the hard ($2-10$ keV) band is shown in blue. One arcmin corresponds to a linear size of 43.7 kpc at the redshift of CTD 86 ($z = 0.037216$). The unresolved source marked "1" is SDSS 142452.11+263715.1 and the source "2" is SDSS J142443.78+263616.2. Source "1" shows broad emission lines in its optical spectrum and is classified as a quasar at $z = 0.3761$. Source "2" is also most likely an AGN.

analysis. The resulting net EPIC-pn, MOS1 and MOS2 exposure times are 30 ks, 30.1 ks and 25 ks, respectively, for the Ob.I and 27.81 ks, 27.12 ks, 27.12 ks for the Ob.II.

We have created (PN+MOS1+MOS2) mosaic image from the Ob.I data set by combining the EPIC-pn, MOS1 and MOS2 event files in the soft ($0.3-1$ keV), intermediate ($1-2$ keV) and hard ($2-10$ keV) bands. We smoothed these images with a Gaussian kernel of radius $10''$ and combined to from a false color image. Figure 3 shows the tri-color X-ray image of CTD 86 and its environment. This image confirms the diffuse soft X-ray emission from CTD 86 and two unresolved X-ray sources near CTD 86 which were detected with *ROSAT* (see § 3.1). In addition, we also find an unresolved core at the center of CTD 86. The core is prominent in the $2-10$ keV band. We have also created a composite X-ray ($0.3-1$ keV band, in blue), SDSS optical (red) and radio FIRST (green) image for CTD 86 and shown in Figure 4. From this figure it is clear that the unresolved X-ray core is at the centre of the galaxy CTD 86. Thus, the hard X-ray at the center of diffuse X-ray emission represents the active nucleus of CTD 86. The radio-lobes of CTD 86 are embedded in the hot gas. Though the signal-to-noise ratio of the diffuse X-ray emission is poor, we do not detect any cavity caused by the interaction of radio-lobes with the surrounding diffuse gas. We also confirm the optical counterparts of two nearby bright X-ray sources. In Figures 3 and 4, the point source

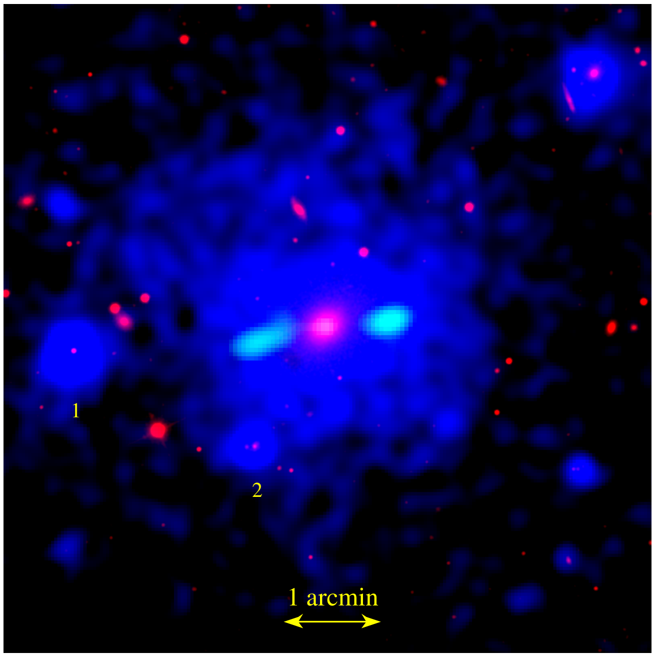

Figure 4. Composite soft (0.3−1 keV) band X-ray (blue), SDSS optical (red) and FIRST radio (green) image of CTD 86 and its environment. The unresolved source marked "1" is SDSS 142452.11+263715.1 and the source "2" is SDSS J142443.78+263616.2. Optical counterparts of the point sources are clearly seen.

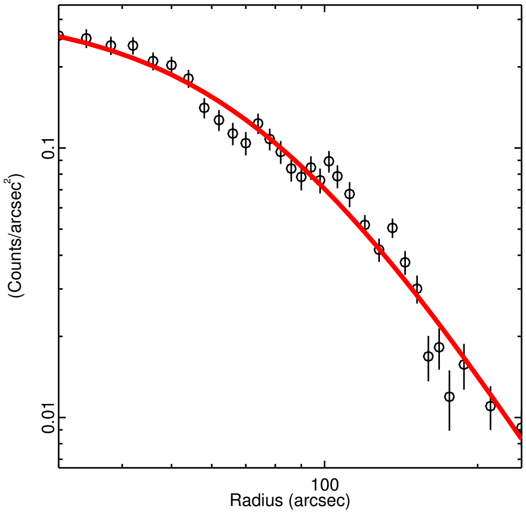

Figure 5. Background subtracted, azimuthally averaged radial surface brightness profile of CTD 86 extracted from the data range 0.3-2.5 keV. The red line shows the best fitted 1d-β model and black points are the extracted photons from each annuli.

marked "1" is SDSS 142452.11+263715.1 and the source "2" is SDSS J142443.78+263616.2. We have listed SDSS u magnitudes of these sources in Table 2.

We have derived a background subtracted, azimuthally averaged, radial profile in the energy range of 0.3-2.5 keV by extracting X-ray photons from concentric circular annuli centered on the CTD 86 and extending up to 360″using *funtool* task available in ds9 application. To avoid contamination due to central point source, we excluded central 15″region. To achieve roughly same S/N on each annulus, particularly in the outer parts, we accordingly adjusted the width of the annuli. From Figure 5, it appears that the extended emission is detectable up to ∼250″(∼ 186 kpc). The surface brightness profile of the CTD 86 is fitted with a single 1-d β model, with the best fit core radius r_c=46.12±4.46 kpc, and slope parameter $\beta = 0.61\pm0.03$. The errors shown here are at 68% confidence levels.

3.2.2 Spectral Analysis

We extracted EPIC-pn, MOS1 and MOS2 spectra of the hot diffuse gas around CTD 86 using a circular region with radius 100″ and excluding two circular regions of radii 30″ and 40″ centered at CTD 86 and the nearby source SDSS J142443.78+263616.2, respectively. We also extracted three EPIC spectra for the nucleus using a circular region with radius 30″ centered at the position of CTD 86 to study the central engine. The background regions were chosen from source-free regions to avoid possible contamination from the hot diffuse gas of CTD86. We also extracted background spectra from nearby source free circular regions. Similarly, we also extracted spectra for the two bright X-ray sources SDSS J142443.78+263616.2 and SDSS J142452.11+263715.1 using circular regions of radii 40 arcsec and appropriate circular, source-free regions for the corresponding background. Ancillary response file (ARF) and redistribution matrix file (RMF) were generated using the SAS tasks `rmfgen` and `arfgen`, respectively. The resulting spectra were binned to a minimum of 30 counts per bin for CTD 86 and SDSS J142443.78+263616.2, and 20 counts per bin for SDSS J142452.11+263715.1. We used the X-ray spectral analysis package XSPEC v12.6.0 (Arnaud 1996) and performed the spectral fitting by minimizing the χ^2. The errors on the fitted parameters are quoted at the 90% confidence level.

We analyzed the EPIC-pn, MOS1 and MOS2 spectral data jointly for each of the three sources. We multiplied all models with a constant component in order to account for possible differences in relative normalizations for the three instruments. The constant component was fixed at 1 for the EPIC-pn data and varied for the MOS1 and MOS2 data.

3.2.3 The diffuse emission

X-ray tri-colour image (Figure 3) shows that CTD 86 has a substantial amount of unresolved or diffuse emission. To study this diffuse emission we extracted and analysed spectra from region 1 as described § 3.2.2 from the Ob.I of CTD 86. We used a single component model `apec`, appropriate for thermal plasma. The `apec` model were modified by the Galactic absorption ($N_H^{Gal} = 1.61 \times 10^{20}$ cm^{-2}). The fit resulted in a minimum $\chi^2 = 386.9$ for 285 degrees of freedom (dof). Examination of the residuals showed the presence of weak excess emission at higher energies and a residual instrumental line at 1.79 keV due to Si Kα. A power-law component and a Gaussian line were used to account for the excess emission and the 1.79 keV line, respectively. The weak power-law component could arise due to the contributions of nuclear emission due to large point spread function or the host galaxy. It could also arise due to incorrect subtraction of background due to soft protons (Snowden et al. 2008; Lakhchaura et al. 2011). The `wabs(apec+powerlw+Gauss)` model improved the fit to $\chi^2/dof = 283.3/280$. We also performed spectral analysis of the data resulting from the Ob.II and found that the data are well described by a similar model. The model `wabs(apec+powerlw+Gauss)` provided the best fitted temperature of the diffuse emission to be $kT = (0.71 \pm 0.02)$ keV and the corresponding diffuse X-ray flux in the $0.3 - 10$ keV band to be $f_X = (15.1 \pm 0.7) \times 10^{-13}$ ergs s^{-1} cm^{-2} for Ob.I and for Ob.II $f_X = (11.7 \pm 0.6) \times 10^{-13}$ ergs s^{-1} cm^{-2}, respectively. We have listed the best-fit parameters of these fits in Table 3 and have plotted the spectral data, the best-fit model and the deviations of the observed data from the best-fitting model in Figure 6. The confidence contours at the 68.3%, 90%, and 99% confidence levels for temperature, abundance and N_H^{intr} for Ob.I and Ob.II are shown in Figure 7. The best fit values for the elemental abundances for both the observations are found to be 0.20 ± 0.02 and 0.22 ± 0.04 relative to the solar value. The X-ray luminosity of CTD 86 in the $0.3 - 10$ keV band is thus derived to be $L_X \sim 4.8 \pm 0.2 \times 10^{42} erg\ s^{-1}$ for Ob.I and $\sim 3.6 \pm 0.2 \times 10^{42} erg\ s^{-1}$ for Ob II, respectively. The electron density of the thermal plasma can be calculated from the normalization of `apec` model,

$$n_{apec} = \frac{10^{-14}}{4\pi[D_A(1+z)]^2} \int n_e n_H dV, \tag{1}$$

where D_A is the angular diameter distance to the source, n_e and n_H are the electron and proton densities, respectively. For CTD 86, using the best-fitted temperature of 0.71 ± 0.02 keV, assuming a uniform gas density within the central $100'' \sim 74.4$ kpc and $n_e \approx n_H$, we find an average electron density $n_e \approx 3 \times 10^{-3}$ cm^{-3} and a total diffuse gas mass $M_{gas} = 1.83 \times 10^{11}\ M_{\odot}$.

3.2.4 The Nuclear X-ray source

Similarly, we carried out the spectral analysis of the central region of CTD 86. As seen in the X-ray tri-colour image (Figure 3), the central region of CTD 86 exhibits a substantial diffuse emission from hot gas as well as X-ray emission from the AGN. Therefore, we used a two component model consisting of `apec`, appropriate for a thermal plasma, and a `powerlaw` for the AGN. Both the components were modified by the Galactic absorption ($N_H^{Gal} = 1.6 \times 10^{20}$ cm^{-2}). The fit resulted in minimum $\chi^2 = 345.7$ for 167 degrees of freedom (dof). Examination of the residuals showed deficit of emission in the $1.5 - 3$ keV band, suggestive of intrinsic absorption of the power-law component. Multiplying the power-law with a `zwabs` component, thus fitting the model `wabs(apec+zwabs`× `zpowerlw)` improved the fit to χ^2/dof 159.8/164. We also performed spectral analysis of the data resulting from the Ob.II and found that a similar model describes the data very well. We have listed the best-fit parameters of these fits in Table 3 and plotted the spectral data, the best-fit model and the deviations of the observed data from the best-fitting model in Figure 6. The confidence contours at the 68.3%, 90%, and 99% confidence levels for temperature, abundance and N_H^{intr} for Ob.I and Ob.II are shown in Figure 7.

The model `wabs(apec + zwabs`× `powerlaw)` provided the intrinsic absorption column $N_H = 5.9^{+0.8}_{-1.0} \times 10^{22} cm^{-2}$ for Ob.I and $N_H = 5.4^{+1.3}_{-1.0} \times 10^{22} cm^{-2}$ for Ob. II, respectively. The intrinsic absorption is among the highest observed from low power FR I galaxies. Donato et al. (2004) observed intrinsic columns in the range $N_H = 10^{20} - 10^{21}$ for their sample of 25 FR I galaxies. On the other hand the power law photon inidices (Γ) for Ob.I and II are of $1.58^{+0.27}_{-0.25}$, $1.54^{+0.29}_{-0.27}$, are similar. The best fit values for the elemental abundances for the hot gas component in both the observations are found to be 0.15±0.05 and 0.14±0.07 relative to the solar value. The temperature of the diffuse emission is 0.89±0.05 keV and corresponding diffuse X-ray flux in the $0.3-10$ keV band is $f_X = (0.66 \pm 0.10) \times 10^{-13}$ ergs s^{-1} cm^{-2} for Ob.I and for Ob.II $f_X = (0.71 \pm 0.12) \times 10^{-13}$ ergs s^{-1} cm^{-2}. The X-ray luminosity of CTD 86 in $0.3 - 10$ keV band is $L_X \sim 2.1 \pm 0.2 \times 10^{42} erg\ s^{-1}$ for Ob.I and $\sim 1.8 \pm 0.3 \times 10^{42} ergs^{-1}$ for Ob. II. Using the best-fit temperature (0.89 ± 0.05) keV, and assuming a uniform gas

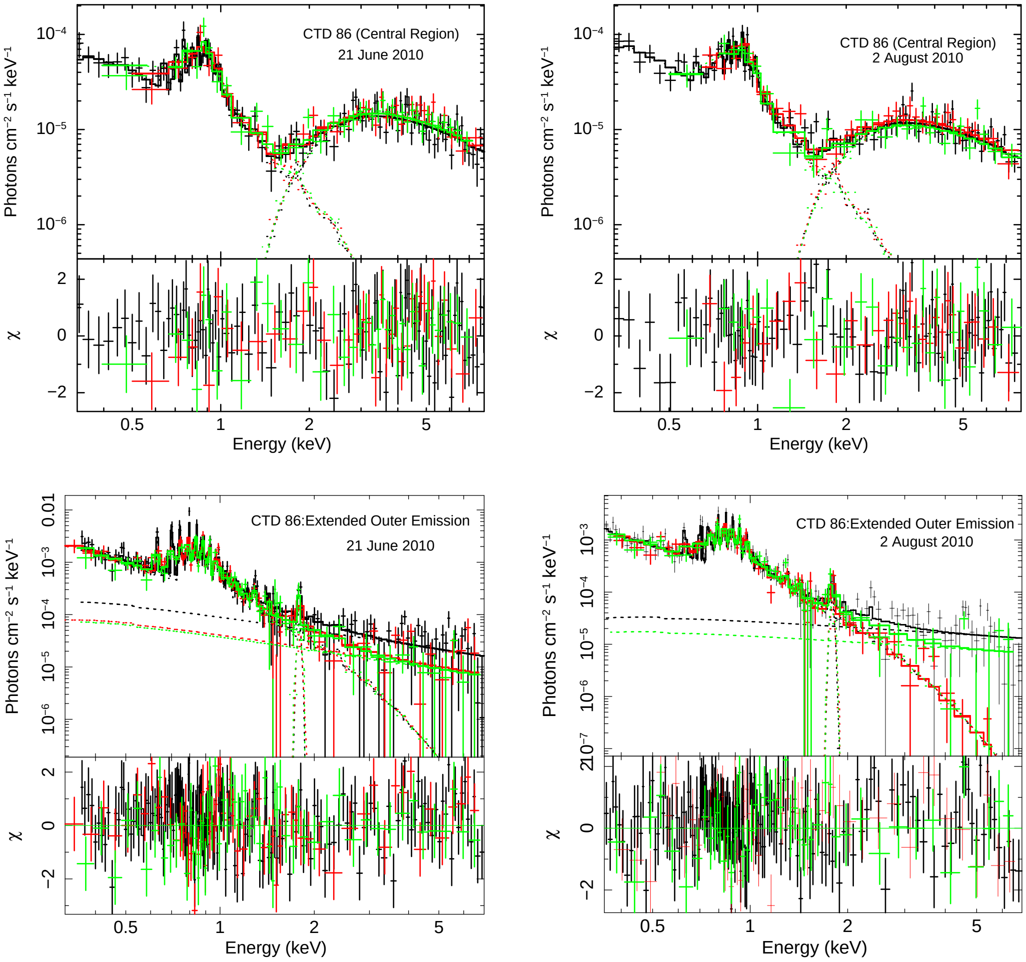

Figure 6. X-ray spectral data, best-fit models and the deviations of the data from the best fit models for CTD 86 from two observations: Ob.I (left) & Ob.II (right).

density within the central 30″∼ 0-22 kpc, gives a density of $n_e \approx 4.4 \times 10^{-3}$ cm^{-3} and a total gas mass $M_{gas} = 5.9 \times 10^9\ M_\odot$.

3.3 Two bright X-ray Sources

Two new bright X-ray sources: SDSS J142452.11+263715.1 and SDSS J142443.78+263616.2 were detected near CTD 86 at a projected distance of 119 kpc and 64 kpc from the centre of CTD 86, respectively, and are shown in Figure 1. In the SDSS DR7 and DR8 data, SDSS J142452.11+263715 has been identified as a star and SDSS J142443.78+263616.2 as a galaxy. Based on our optical identification and analysis of the SDSS optical spectrum, we find that the star-like object SDSS J142452.11+263715 is a broad emission line quasar with $z = 0.3761$ (see also § 5 & Figure 9 right panel). The nature of SDSS J142443.78+263616.2 is not clear as its optical spectrum is not available. This object is extended in the SDSS image and is likely to be a galaxy harboring an AGN.

Table 3. Results of X-ray spectral modeling of CTD 86 for Ob.I & Ob.II.

Parameter	Nuclear		Diffuse	
Model	wabs(apec+zwabs×ZPL)		wabs(apec+PL+Gauss)	
	Ob.I (21 June 2010)	Ob.II (2 Aug. 2010)	Ob.I (21 June 2010)	Ob.II (2 Aug. 2010)
$N_H^{Gal}(10^{20}\ \mathrm{cm}^{-2})$	1.6(fixed)	1.6(fixed)	1.6(fixed)	1.6(fixed)
kT_{apec}(keV)	0.89 ± 0.05	0.89 ± 0.07	0.71 ± 0.02	0.74 ± 0.01
Abundance (× solar)	0.15 ± 0.05	0.14 ± 0.07	0.20 ± 0.02	0.22 ± 0.04
$f_X^{apec}(0.3 - 10\ \mathrm{keV})^a$	0.66 ± 0.10	0.71 ± 0.12	15.1 ± 0.7	11.7 ± 0.6
$N_H^{intr}(10^{22}\ \mathrm{cm}^{-2})$	$5.9^{+0.8}_{-1.0}$	$5.4^{+1.3}_{-1.0}$	–	–
Γ	$1.58^{+0.27}_{-0.25}$	$1.54^{+0.29}_{-0.27}$	0.26 ± 0.4	0.98 ± 0.6
Si Kα G_{line}(keV)	–	–	1.77 ± 0.03	1.77 ± 0.04
$\sigma(gauss)$(keV)	–	–	4.01×10^{-4}	4.07×10^{-4}
f Si Kα^b	–	–	$6.62 \pm 4.62 \times 10^{-6}$	$4.61 \pm 3.39 \times 10^{-6}$
$f_X^{PL}(2 - 10\ \mathrm{keV})^a$	$8.3^{+0.9}_{-1.6}$	$6.7^{+0.5}_{-0.4}$	–	–
χ^2/dof	159.8/164	134.9/140	283.3/280	250.3.9/258

[a] In units of 10^{-13} ergs cm^{-2} s^{-1}.
[b] Line flux in photons keV^{-1} cm^{-2} s^{-1}.

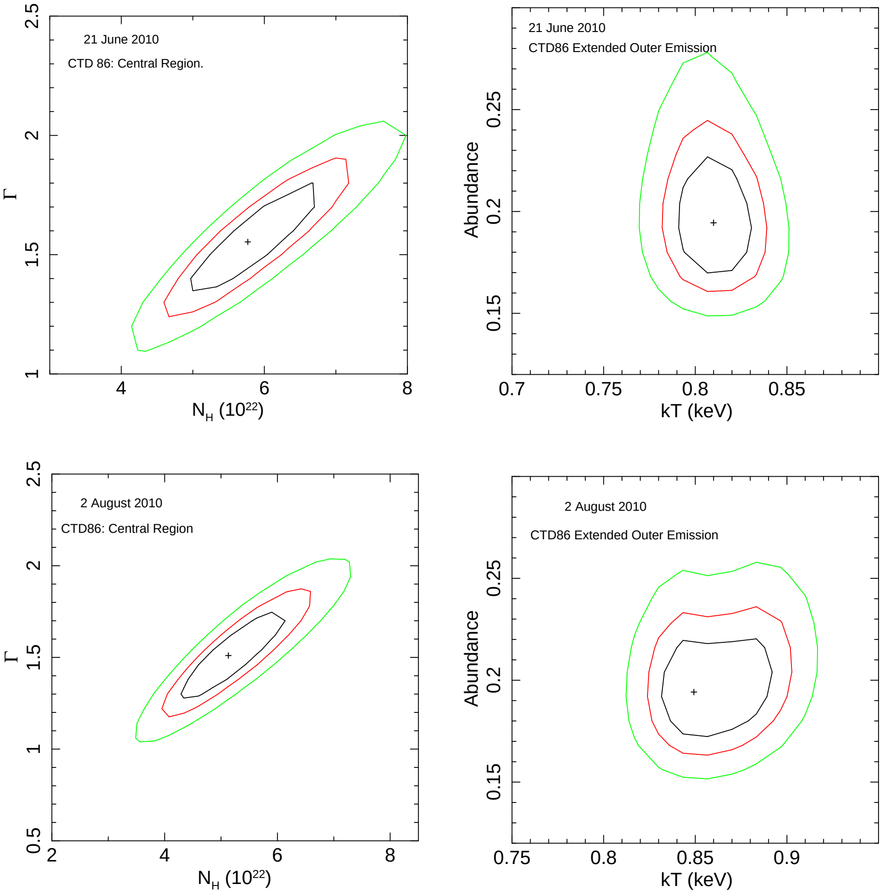

Figure 7. *Top left panel:* χ^2 contours of the photon index, N_H^{intr} measurements for the central 30″regions of CTD 86, *top right panel:* χ^2 contours of the temperature and abundance measurements for the 100″region excluding central 30″from the spectral analysis done using Chandra data for Ob.I. *bottom left panel:* χ^2 contours of the photon index, N_H^{intr} measurements for the central 30″regions of CTD 86. *bottom left panel:* χ^2 contours of the temperature and abundance measurements for the 100″region excluding central 30″from the spectral analysis done using Chandra data for Ob.II . The confidence levels for the innermost, middle, and outermost contours are at 68.3%, 90%, and 99%, respectively.

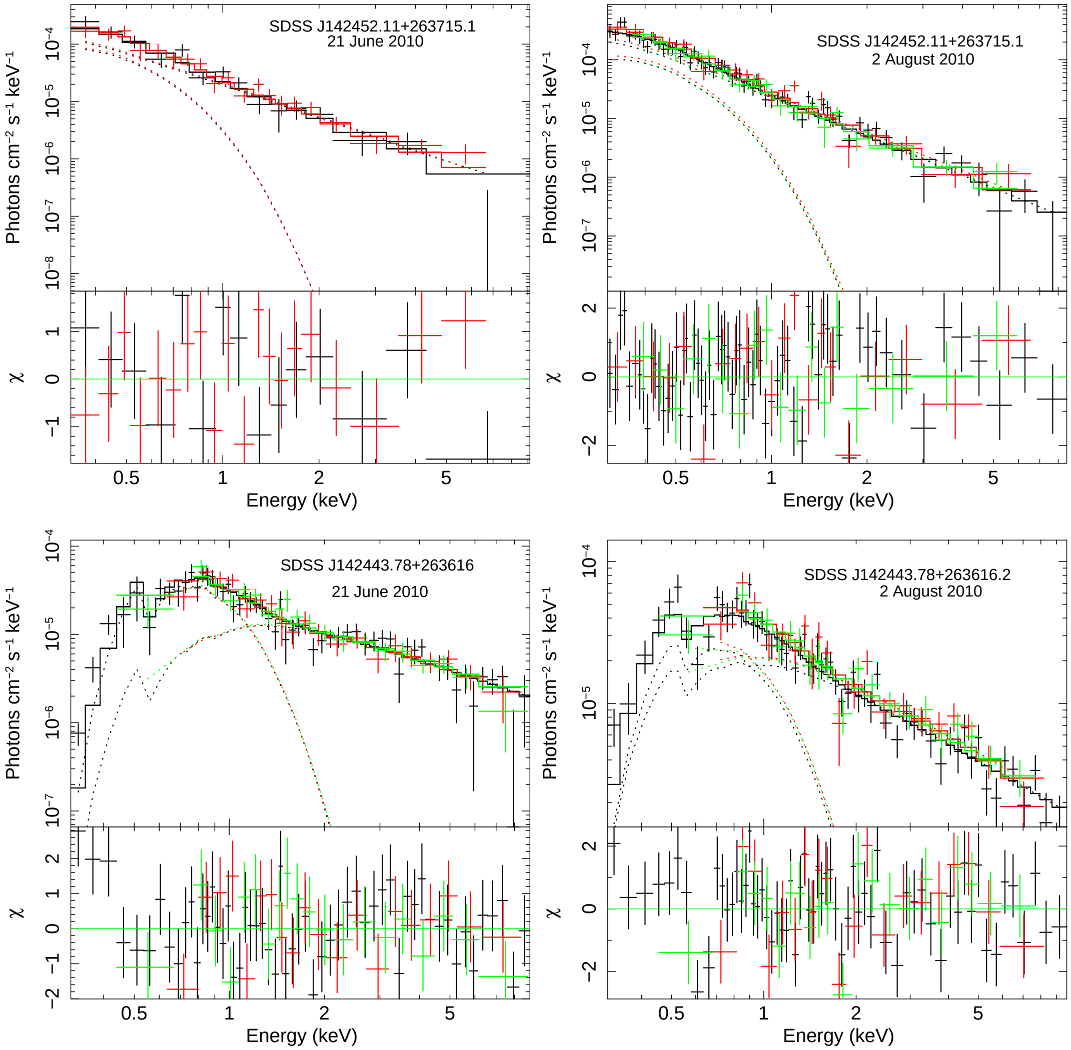

Figure 8. X-ray spectral data, best-fit models and the deviations of the data from the best fit models for SDSS J142452.11+263715.1 and SDSS J142443.78+263616.2 from two observations: Ob.I (left) & Ob.II (right).

Table 4. Best-fit spectral model parameters of the two nearby point sources for Ob.I & Ob.II

Parameter	SDSS J142452.11+263715.1		SDSS J142443.78+263616.2	
Model	wabs(ZBB+ZPL)		wabs*wabs(BB+PL)	
	Ob.I (21 June 2010)	Ob.II (2 Aug. 2010)	Ob.I (21 June 2010)	Ob.II (2 Aug. 2010)
$N_H^{Gal}(10^{20}\ \mathrm{cm}^{-2})$	1.6(fixed)	1.6(fixed)	1.6(fixed)	1.6(fixed)
kT_{BB} (keV)	$0.15^{+0.04}_{-0.07}$	$0.14^{+0.02}_{-0.04}$	$0.13^{+0.04}_{-0.02}$	$0.17^{+0.07}_{-0.04}$
$f_X^{BB}(0.3-10\ \mathrm{keV})^a$	$0.23^{+0.17}_{-0.19}$	$0.24^{+0.13}_{-0.15}$	$2.3^{+7.4}_{-1.7}$	$0.6^{+1.6}_{-0.3}$
$N_H^{intr}(10^{22}\ \mathrm{cm}^{-2})$	–	–	$0.36^{+0.22}_{-0.20}$	$0.16^{+0.34}_{-0.09}$
Γ	$1.95^{+0.34}_{-0.35}$	$2.22^{+0.23}_{-0.23}$	$1.20^{+0.21}_{-0.20}$	$1.24^{+0.18}_{-0.18}$
$f_X^{PL}(2-10\ \mathrm{keV})^a$	$0.55^{+0.19}_{-0.16}$	$0.43^{+0.10}_{-0.09}$	2.5 ± 0.3	2.5 ± 0.2
χ^2/dof	30/30	105/98	83/89	125/98

[a] In units of 10^{-13} ergs $\mathrm{cm}^{-2}\mathrm{s}^{-1}$.

To further investigate the nature of these sources, we have performed X-ray spectral analysis. We extracted source spectra from the filtered EPIC-pn and MOS event files using circular regions of 40″radii centered at the source positions. We also extracted the corresponding background spectra from nearly circular regions in the source-free areas. The source SDSS J142452.11+263715.1 falls in the CCD gap in the EPIC-pn data of Ob.I, hence the EPIC-pn spectrum was not useful. The rest of the five spectra from Ob.I and II were grouped to get minimum counts of 20 per energy bin. As before, we performed joint spectral analysis of available spectral data from different instruments for each observation.

We found that the spectra of SDSS J142452.11+263715.1 for each observation are well fitted by a black body plus power-law model modified by the Galactic absorption ($N_H^{Gal} = 1.6 \times 10^{20}$ cm^{-2}). The best-fit parameters are listed in Table 4 for both the observations. The X-ray spectrum of SDSS J142452.11+263715.1 consisting of soft X-ray excess, described as blackbody with $kT \sim 150$ eV, and a powerlaw with $\Gamma \sim 2$, is typical of the spectra of radio-quiet quasars e.g., PG quasars. The total X-ray luminosity of SDSS J142452.11+263715.1 in the $0.3-10$ keV band is L_X is $\sim 6.6 \pm 0.3 \times 10^{43} erg\ s^{-1}$ for Ob.I and $\sim 6.8 \pm 0.25 \times 10^{43} erg\ s^{-1}$ for Ob.II. The best fitted spectra of SDSS J142452.11+263715.1 for both the observations are shown in Figure 8.

The second object, SDSS J142443.78+263616.2, has no redshift information. This source shows soft X-ray emission. Initially we used a model `wabs`×`wabs(apec+PL)`, where thermal plasma model `apec` is for the soft excess and powerlaw for the hard continuum and multiplied both the components by the absorption component `wabs`. We varied the redshift parameter in `apec`. The fit resulted in $\chi^2/dof = 132/88$ and the best-fit redshift $z = 1.50 \pm 0.05$, which may not be correct. Next, we fitted the `wabs`×`wabs(BB+PL)` model, which resulted in $\chi^2/dof = 83.70/89$, $125/98$ for Ob.I and II, respectively. The best-fit parameters are $kT_{BB} \sim 150$ eV and $\Gamma \sim 1.2$ for both the observations. The best fitted spectra of SDSS J142443.78+263616.2 for Ob.I and II are shown in Figure 8 and the spectral fitting parameters are listed in Table 4.

4 OPTICAL IMAGING & SPECTROSCOPY

We have used IRAF[1] software package for the basic reduction and analysis of CCD images. An average bias frame, constructed from multiple bias frames taken very close to the galaxy observation, was subtracted from the object frame and flat field frames. The pixel-to-pixel response variation in the object frames were corrected by dividing the object frame by a master flat frame. The master flat frame was obtained by averaging the best flat frames and normalizing by the mean intensity level of the averaged frame. Cosmic ray events, seen as few isolated bright pixels, were removed by replacing them with the average intensity of four nearest neighbors. The pixel coordinates in the object image were converted into the standard equatorial coordinates for the epoch J2000. The plate solutions were computed by fitting a quadratic polynomial between the known celestial coordinates and pixel coordinates of stars nearby to the object after projecting the celestial coordinates onto the plane tangent to the object center. The bias-corrected and flat-fielded B band image of CTD 86 overlaid with contours of *ROSAT* HRI X-ray surface brightness is shown in Figure 1.

---

[1] IRAF is distributed by the National Optical Astronomy Observatories, which is operated by the Association of Universities, Inc. (AURA) under cooperative agreement with the National Science Foundation.

We have measured optical emission line parameters of CTD 86 and SDSS J142452.11+263715.1 using optical spectroscopic observations available in the archive of the Sloan Digital Sky Survey[3] (SDSS). The optical spectrum and the $H\alpha$ emission line region of the spectrum of CTD 86 are shown in the left panel of Figure 9. As can be seen in the figure, the Balmer $H\alpha\lambda6564$ Å line is blended with forbidden lines[N II]$\lambda6548$ Å and [N II]$\lambda6583$ Å. and the Balmer $H\beta$ emission line is very weak. We have measured the parameters of the strongest emission lines by fitting Gaussian profiles and by minimizing χ^2 . The lines fitted were H_α, [N II]$\lambda6583$ Å, [S II]$\lambda\lambda6716, 6731$ Å and [O I]$\lambda6300$ Å. The best-fit emission line parameters were determined by fixing central wavelengths of all emission lines to their laboratory wavelengths. The best-fitting Gaussian profiles to the data are shown in a box in set Figure 9. We have listed the best-fit emission line parameters in Table 5. The FWHM of the $H\alpha$ line is similar to those of forbidden lines [N II], and [S II] within the errors. This demonstrates that only a narrow component of H_α is present in the spectrum of CTD 86. In many AGN, e. g., Type 1, intermediate Seyfert nuclei, and broad line radio galaxies, the presence of narrow and broad line regions are inferred from the narrow and broad components of Balmer lines. The FWHMs of the narrow component of Balmer lines and those of forbidden lines are usually found to be similar. Thus CTD 86 is a narrow-line radio galaxy. The flux ratio of the [N II]$\lambda6583$ Å line to narrow H_α line, $\frac{[NII]\lambda6583}{F(H_\alpha\lambda6563)}$ is 2.29± 0.13. Similarly, the flux ratio, $\frac{F([SII]\lambda\lambda6716,6731)}{F(H_\alpha\lambda6563)}$ is 1.4±0.1 for CTD 86. The FWHM of the narrow components of $H\alpha$ and [N II] is 535 km s^{-1} and 612 km s^{-1}, respectively. These values of FWHM are similar to

---

[3] SDSS is the Data base http://www.sdss.org

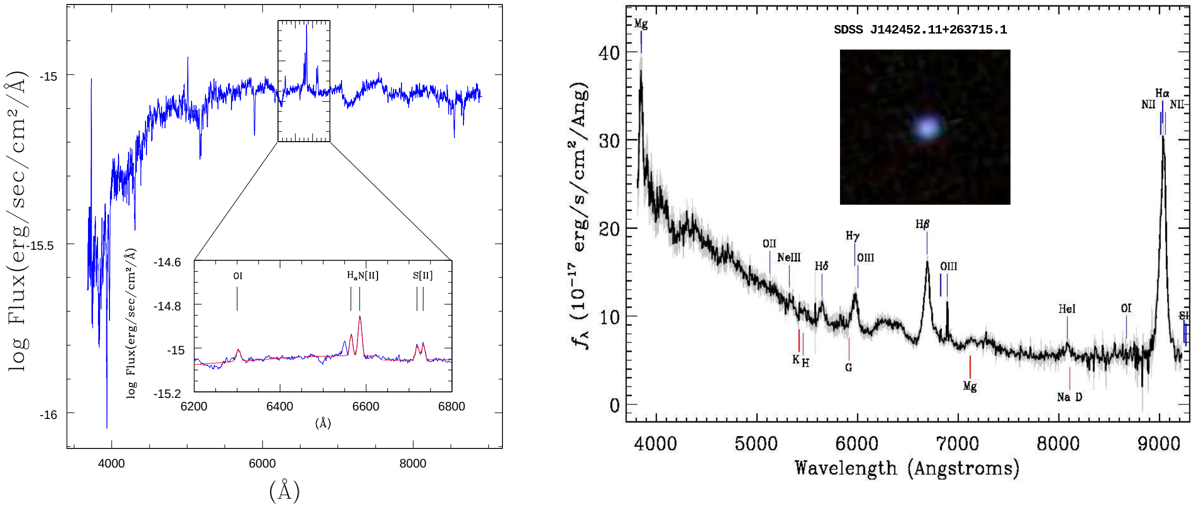

Figure 9. Left panel: The optical spectrum of CTD 86 (blue data points). The emission lines seen in small box are fitted by Gaussian profile to get integrated flux of emission lines. The best fitted data with Gaussian profile shown in second box and fitted lines are marked with their names. Right panel: The color composite image and optical spectrum of quasar SDSS J142452.11+263715.1 obtained from SDSS DR8 release

Table 5. Optical emission line parameters

Parameter	CTD 86		SDSS J142452.11+263715.1	
	flux ($\times10^{-15} ergs\ cm^{-2} s^{-1}$)	FWHM (km s^{-1})	flux ($\times10^{-15}$ergs cm^{-2} s^{-1})	FWHM (km s^{-1})
Hα	2.30 ± 0.11	535	16.2 ± 1.98	3591
[S II]λ6716	1.47 ± 0.12	547	–	–
[S II]λ6731	1.49 ± 0.09	513	–	–
[N II]λ6583	5.09 ± 0.12	612	8.65 ± 3.06	336
[O I]λ6300	0.98 ± 0.09	558	–	–
Hβ	–	–	4.17 ± 0.15	3812
[O III]λ5007	3.13 ± 0.09	664	0.36 ± 0.12	441

those seen in Seyfert 2 nuclei. The flux ratio of the [N II]λ6583 line and narrow component of Balmer H_α line, $\frac{[NII]\lambda6583}{H_alpha\lambda6563}$ is 2.20± 0.62. Similarly, the flux ratio, $\frac{[SII]\lambda\lambda6716,6731}{H\alpha}$ is 1.28±0.11 for CTD 86. The total $H\alpha$ luminosity of CTD 86 is $7.1 \times 10^{39} ergs^{-1}$.

We have also measured the central stellar velocity dispersion for CTD 86 using the available SDSS spectrum. Galaxy stellar kinematics were extracted from the absorption-line spectra of CTD 86 using Penalized Pixel-Fitting method (Cappellari & Emsellem 2004). We used the wavelength range $4795 - 5765$ Å and fitted the template galaxy spectra for CTD 86 . We obtained the best-fit value for the dispersion velocity $\sigma = 182.2 \pm 7.8$ km s^{-1}, and calculated the black hole mass, $M_{BH} = (8.8 \pm 2.4) \times 10^7$ M$\odot$, using the well established $M - \sigma$ relation for nearby galaxies (Gültekin et al. 2009).

We have also analyzed the optical spectrum for the quasar SDSS J142452.11+263715.1 by fitting multiple Gaussian profiles to the emission lines. From Figure 9 (right hand panel),

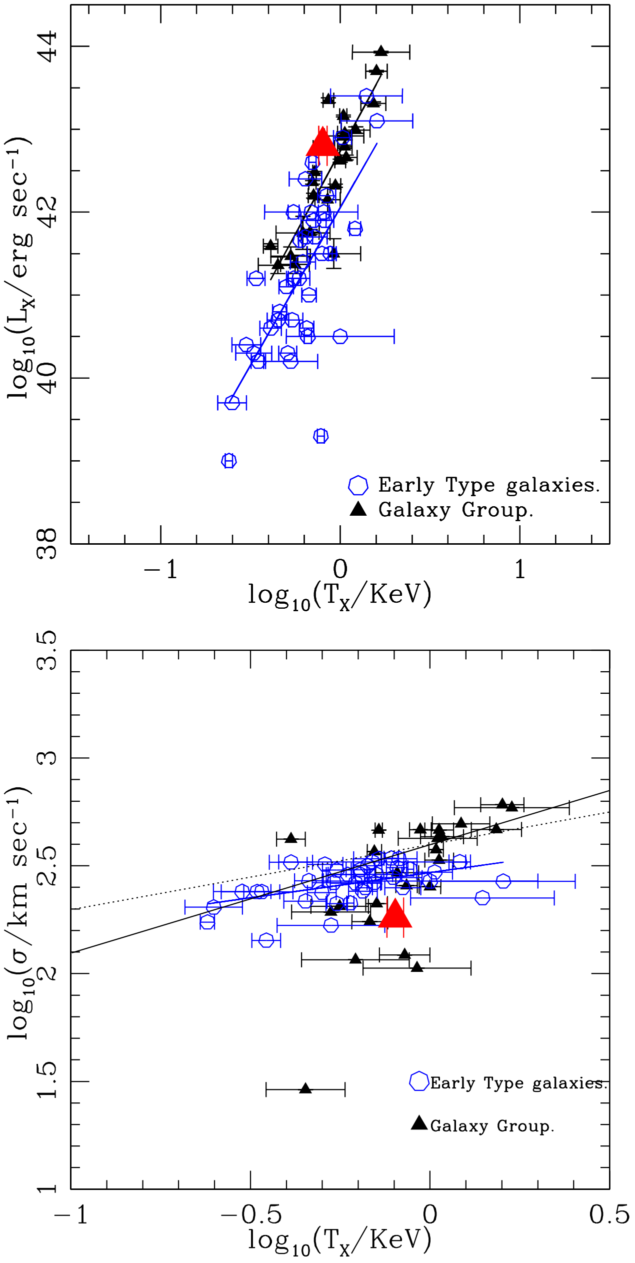

Figure 10. Left panel: Logarithm X-ray luminosity of diffuse gas, L_X plotted against the temperature for a sample of early type galaxies shown as open circles from O'Sullivan et al. (2003) and group of galaxies shown in filled triangles from Helsdon & Ponman (2000). The best fit to the each data shown in solid lines. CTD 86 is shown as big filled triangle. Right panel: Logarithm of the X-ray temperature T_X versus logarithm of optical velocity dispersion σ for a sample of early type galaxies open circles and groups of galaxies filled triangles. The group data are taken from the literature Helsdon & Ponman (2000), with the addition of early type galaxies from in O'Sullivan et al. (2003). The best fit to the data shown in solid line and dashed line represents region where $\beta_{spec} = 1$. CTD 86 is shown as the filled triangle in red color.

one can see that, the Balmer H_α line is heavily blended with forbidden lines [N II]λ6545 Å and $[NII]\lambda6583$ Å. The forbidden emission line doublet $[SII]\lambda6716$ Å, $\lambda6731$ Å is out of SDSS spectral coverage. The best fitted FWHM of the Balmer H_α and H_β emission lines are 3591 km s^{-1} and 3812 km s^{-1}, respectively. The forbidden lines [O III] and [N II] are narrow with FWHM 441 km s^{-1}, 336 km s^{-1}, respectively (see Table 5).

5 DISCUSSION

We have presented the results of our analysis of the *ROSAT* and *XMM-Newton* X-ray imaging and spectroscopy of CTD 86 and its environment. We have also analysed the optical spectra of CTD 86 and a background quasar SDSS J142452.11+263715.1. CTD 86 has a clear a narrow emission line region as is evident from its optical spectrum and it is nucleus of an elliptical host galaxy. The emission line widths and intensity-ratios are typical of type 2 AGNs. Ho et al. (1997) have defined the low luminosity or dwarf AGNs to be those with $L_{H\alpha} \leqslant 10^{40}$ erg s^{-1} and $\frac{[\mathrm{N\ II}]\lambda6583\mathring{A}}{H\alpha} \geqslant 0.6, \frac{[SII]\lambda\lambda6716,6731}{H\alpha\lambda6563} \geqslant 0.4$, and $\frac{[OI]\lambda6300}{H\alpha\lambda6563} \geqslant 0.08$ (Seyfert) or 0.17 (LINER's). The $H\alpha$ luminosity of CTD 86 is about a factor of four smaller than those for the low luminosity AGN's. The flux ratios $\frac{[NII]\lambda6583}{H\alpha\lambda6563}$, and $\frac{F([SII]\lambda\lambda6716,6731)}{H\alpha\lambda6563}$ for CTD 086 are much higher than limiting flux ratios set by Ho et al. 1997 . The forbidden line [O I]λ6300 Å is clearly seen and could be identified in the spectrum of CTD 86. The flux ratio for $\frac{[O\ I]\lambda6300}{H\alpha\lambda6563}$ of CTD 86 is probably more like that for a Seyfert nuclei than for a low ionization nuclear emission region (LINER) galaxy.

5.1 The Diffuse X-ray Emission

CTD 86 shows extended X-ray emission with linear size $\sim 250'' \sim$ 186 kpc in the *XMM-Newton* observations. This confirms the diffuse emission previously detected with the *ROSAT* HRI observations (Canosa et al. (1999)). Here we have explored the origin of the diffuse X-ray emission as discussed below.

The diffuse X-ray emission detected with the *XMM-Newton* and presented here is well described by thermal emission from hot gas with temperature $kT = 0.71 \pm 0.02$ keV, electron density $n_e \sim 3 \times 10^{-3}$ cm^{-3}, X-ray luminosity $L_X = 4.8 \pm 0.2 \times 10^{42}$ erg s^{-1}, with $0.3-10$ keV energy band. These values suggest its origin either from a group of galaxies or a poor cluster.

It has been clear from various observations that there is a strong correlation between the X-ray luminosity L_X and X-ray temperature T_X of the groups and galaxy clusters (Xue & Wu 2000). We have compared CTD 86 X-ray luminosity and temperature with those of early type galaxies, groups and cluster members and are presented in Figure 10 (left panel). For this comparison we have taken L_X and kT_X values of early type galaxies from (O'Sullivan et al. 2003) (blue open circles) and group of galaxies taken from Helsdon & Ponman (2000) (filled black triangles). We have also shown CTD 86 in the same plot as filled red triangle. From this figure it is clear that the temperature and luminosity of CTD 86 are consistent with the $L_X - T_X$ relation for both early-type galaxies and groups.

The T_X of the ICM/IGM medium and the σ of the galaxies provide a measure of the gravitational potential and hence, a correlation between these two quantities is expected (Mulchaey 2000). We have compared the X-ray diffuse gas temperature kT_X and the dispersion velocity σ for CTD 86 with the samples of early type galaxies from O'Sullivan et al. (2003) and groups from Helsdon & Ponman (2000). Figure 10 (right panel) shows the $\sigma - T_X$ relation. CTD 86 appears to be consistent with the $\sigma - T_X$ relation of both the early-type galaxies and the groups, it occupies a location more appropriate for groups. In the Figure 10 (right panel), CTD 86 is slightly off from the β_{spec}=1 line(shown as the dotted line). Here, β_{spec}=1 is defined as the ratio of the specific energy in the galaxies to that in the gas. From Figure 10 (right panel), we can conclude that there may be an indication that some excess energy has been injected in this system, which is in agreement with the effects of pre-heating by galaxy winds (Helsdon & Ponman 2000).

The X-ray luminosity L_X of optically luminous galaxies is correlated with their optical luminosity L_B. This could be a manifestation of proportionality between stellar mass of a galaxy (traced by L_B) and stellar velocity dispersion of that galaxy (traced by L_X) (Mahdavi & Geller 2001). The derived X-ray emitting gas temperature is ∼1 keV, as expected from the hot gas trapped and heated in the weak gravitational potentials of early type galaxies (Georgantopoulos & Georgakakis 2005). For CTD 86, the B band and K_s band luminosities are $L_B = Log10.11 L_{B\odot}$ and $L_K = Log10.46 L_{B\odot}$ as listed in the NED [4]. We have compared our diffuse gas luminosity L_X with B band luminosity L_B with best fitting relation for early type galaxies studied by (e.g., O'Sullivan et al. 2001). In Figure 11, we have plotted L_X versus L_B for a sample of early type galaxies studied by (O'Sullivan et al. 2001) and (O'Sullivan et al. 2001) shown as black hexagon and blue triangles, respectively. The solid continuous line is the best-fit line to the (O'Sullivan et al. 2001) excluding the AGN, bright cluster galaxies and dwarfs. The dashed lines are the 1σ deviation around the best-fit line. The filled triangle (red) represents CTD 86. In this Fig. 11, CTD 086 lies well above the best fitting relation found by O'Sullivan et al. (2001), thus indicating that the diffuse X-ray emission in CTD 86 is more likely to originate from a rich group rather then from an isolated galaxy. This is reminiscent of extended diffuse emission seen around massive ellipticals in clusters of galaxies (e.g., O'Sullivan et al. 2003; Paolillo et al. 2003).

---

[4] https://www.nedwww.ipac.caltech.edu

In addition to measuring the gas temperature, we have also estimated the metal content of CTD 86. The distribution of group temperatures is found to occupy a small range around ∼1 keV and the weighted mean metallicity is found to be 0.19±0.01 solar for the sample studied by Helsdon & Ponman (2000) . The metallicity of ~ 0.20 solar for CTD 86 obtained from the best fitted spectra closely matches with those obtained by Helsdon & Ponman (2000).

A strong correlation is also found between X-ray luminosity and velocity dispersion in groups. X-ray luminosity L_X is nearly proportional to σ^4 (Plionis & Tovmassian 2004; Ortiz-Gil et al. 2004; Brough et al. 2006). Helsdon & Ponman (2000) have shown that the L_X: σ correlation for groups was basically consistent between the loose and compact groups. It was, however, noted by Mahdavi et al. (2000) that the relationship may become somewhat flatter for low velocity dispersion systems. In Figure 12, we have plotted L_X against σ for the sample of Helsdon & Ponman (2000) and show CTD 86 as a filled triangle in red color. A strong correlation between L_X and σ is seen, however, CTD 86 is slightly offset from the correlation line.

We have tried to identify other members of a possible group around CTD 86. However, the redshift information is not available for nearby objects except for the quasar at $z = 0.3761$ which is a background quasar. In summary, all the correlations L_X:T, σ:T, L_X:σ, L_X:L_B described above provide clues that the extended diffuse emission seen in the CTD 86 is similar to that of group of galaxies rather than an isolated galaxy.

5.2 The Active Nucleus of CTD 86

X-ray emission from the low luminosity AGN in CTD 86 is well described by a power-law ($\Gamma = 1.58 \pm 0.3$) modified by intrinsic absorption with $N_H = 5.9^{+0.8}_{-1.0} \times 10^{22}$ cm^{-2}. Donato et al. (2004) observed a range of photon indices, $\Gamma = 1.1 - 2.6$, and intrinsic absorption column densities, $N_H = 10^{20} - 10^{21}$ cm^{-2} for AGNs in FR I galaxies. Thus, the non-detection of a central point source with *ROSAT* is not surprising due to the presence of intrinsic absorption and the softer energy response of the *ROSAT* HRI. The $2 - 10$ keV luminosity of the active nucleus is only $L_X \sim 2 \times 10^{42}$ ergs s^{-1}, making CTD 86 a low luminosity AGN. Thus, the weakness of the emission line spectrum could be due to a weak

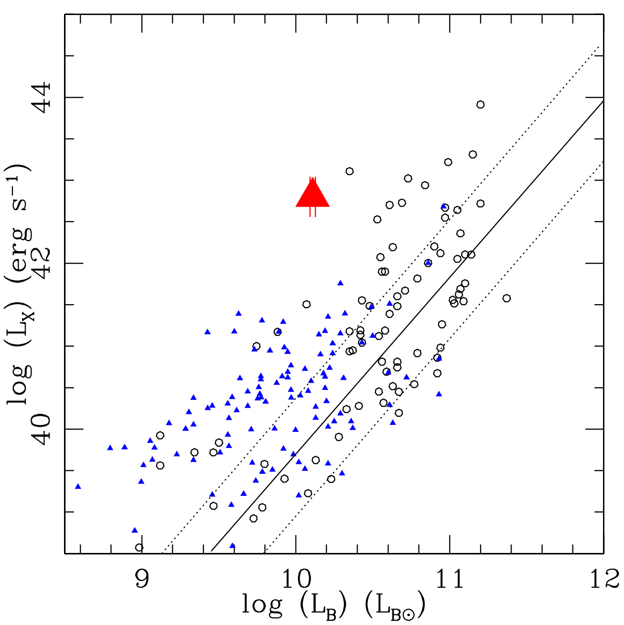

Figure 11. Logarithm of L_X versus Logarithm of L_B for a sample of early type galaxies presented by (O'Sullivan et al. 2001) open hexagon (black) and filled triangles (blue) represent detection and upper limits in the (O'Sullivan et al. 2001). The solid continuous line is the best fit line to the (O'Sullivan et al. 2001) excluding the AGN, bright cluster galaxies and dwarfs. The dashed lines are the 1 σ detection around the best fit line. The filled triangle (red) represent CTD 86.

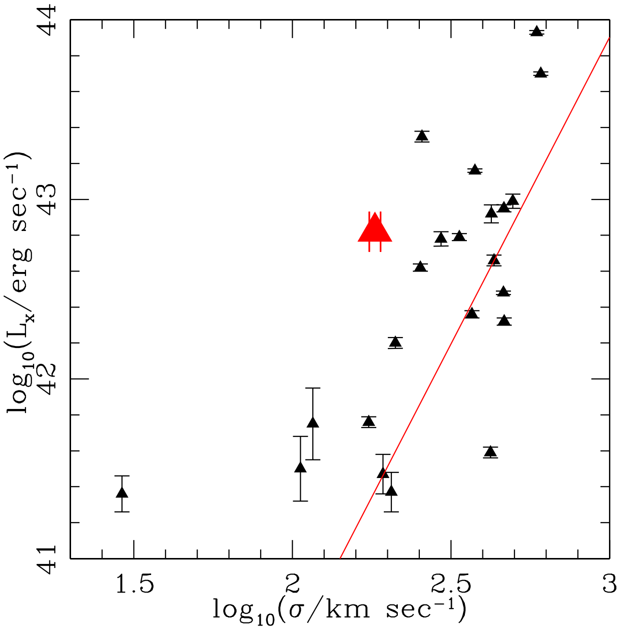

Figure 12. Logarithm of L_X versus Logarithm of σ for a sample of X-ray bright groups of galaxies filled triangles (black). The filled triangle (red) represents CTD 86. The data are taken from Helsdon & Ponman (2000)

nuclear X-ray emission. Photo-ionization by a diluted power law nuclear emission seems to be the appropriate ionization mechanism to account for the observed optical emission lines from CTD 86. The power-law photon index of CTD 86 is within the range of that observed for AGN in FR I galaxies by Donato et al. (2004). However, the intrinsic absorption column density for CTD 86 is the highest observed for any FR I galaxy. Based on the low column densities observed in their sample of FR I galaxies, Donato et al. (2004) concluded that most FR I galaxies lack a standard torus. Since ISM of elliptical galaxies are unlikely to provide absorbing columns more then 10^{21} cm^{-2}, CTD 86 provides an intriguing possibility of the presence of a torus in an FR I galaxy. VLBI imaging of CTD 86 has shown symmetric jets on kpc scale and a possible one-sided jet on parsec scale (Giovannini et al. 2005). Assuming the parsec scale structure to be real, Giovannini et al. (2005) estimated an inclination angle $\theta = 45 - 50\,\deg$ and $beta = 0.95$. X-ray absorption column of $N_H \sim 5.9 \times 10^{22}$ cm^{-2} in CTD 86 is similar to the absorption columns usually observed for intermediate type Seyfert galaxies (e.g., Seyfert 1.5). Thus, the absorption column and the tentative inclination angle both are consistent with the presence of a torus where the line of sight to the nucleus passes through the outer region of the torus.

It is interesting to investigate further if the disk-corona geometry in CTD 86 is similar to that in type 1 radio-quiet AGN such as Seyfert 1 galaxies. We have measured the stellar velocity dispersion $\sigma = 182 \pm 8$ km s^{-1} of CTD 86 from the SDSS spectrum and calculated a black hole mass, $M_{BH} = (8.8 \pm 2.4) \times 10^7$ M$_\odot$ using the $M_{BH} - \sigma$ relation. We estimated the bolometric luminosity from the $2-10$ keV luminosity assuming a bolometric correction of 20 (e.g., Vasudevan & Fabian 2007). This resulted in a relative accretion rate, $\dot{m} = L_{bol}/L_{Edd} \sim 4 \times 10^{-3}$ which is quite low compared to that found for typical Seyfert and quasars. One way to find the relative contributions of disk and corona is to compare the ratio of luminosities of [O III]λ5007 line and the unabsorbed $2-10$ keV luminosity. The strength of the [O III] line would depend on the ionizing flux i.e., emission from the accretion disk, while the power-law X-ray emission arises from a hot corona. Donato et al. (2004) have found an average value of $L_X/L_{[O\ III]}$ to be 27.8 ± 9.6 for Seyfert 1 galaxies and 3.7 ± 1.1 for Compton thick Seyfert 2 galaxies and the lack of X-ray emission from Seyfert 2 galaxies is attributed to absorption by Compton-thick tori. We find a very large ratio, $L_X/L_{[O\ III]} = 354$, for CTD 86. The [O III]λ5007 line is a good indicator of isotropic ionizing luminosity. The very large ratio for CTD 86 either suggests a beamed X-ray emission arising from a jet or a lack of ionizing luminosity from the accretion disk. The first possibility, i.e. the jet origin, is unlikely as the X-ray emission is absorbed by a high column density ($N_H \times 10^{22}$ cm^{-2}) matter. The second scenario is possible only if the accretion disk is truncated so that inner disk does not exist and there is no ionizing radiation from the hottest part of the disk. The inner region below the truncation radius may be filled with a hot flow that gives rise to the observed X-ray emission. The inner hot flow may also be responsible for the radio jets.

5.3 Interaction of the Radio Jets with the Hot Gas

CTD 86 is a low luminosity radio galaxy with classical double-lobed radio emission. Figure 2 shows that the lobes extend to $\sim$ 65 kpc from the optical center of the galaxy and the entire radio source is well contained in the hot X-ray emitting gas. Since it is believed that the double-lobed radio emission arises from the interaction of relativistic electrons with the surrounding magnetic field, and the relativistic high energy electrons are fed by the twin-jets which originate from the active nucleus, therefore, the observed radio structure is another evidence for the presence of an active nucleus in CTD 86. The large scale radio structure of radio galaxies is thought to be at least partly determined by the interactions with the surrounding hot gas. Similarly, the distribution of hot gas in groups and clusters is also affected by the presence of radio jets and lobes. Several example of cavities in the distribution of X-ray gas, coinciding with the locations of radio lobes have been observed with *Chandra* and *XMM-Newton* (e.g, McNamara & Nulsen 2007). In CTD 86, radio lobes are embedded in the hot gas but we see no clear evidence of distortions in the radio structure. There is no clear evidence for X-ray cavities at the locations of the radio lobes although the present result is not sufficient to make this a definite conclusion. Croston et al. (2005) studied radio source heating in groups and found that the gas around the radio-loud AGN is more likely to be hotter at a given X-ray luminosity compared to the gas in radio-quiet groups. We have compared X-ray luminosity and temperature of extended gas around CTD 86 with that of other radio loud and radio quiet galaxies of similar type. In Figure 13 (left hand panel), $\log L_X$ plotted against the $\log T_X$ for the sample of galaxies taken from Croston et al. (2005). The filled triangles (black) represent data points for radio loud sample and filled circle (blue) represent sample of radio quiet galaxies. In the same plot, the red hexagon point shown represents CTD 86. This plot shows many radio-loud groups lying below the best-fit line for radio-quiet groups. However, the temperature and luminosity of the hot gas in the CTD 86 environment is consistent with the $L_X - T$ relation for radio-quiet AGN. The difference in the gas properties of radio-loud and radio-quiet groups can be interpreted as an evidence for heating by radio-source (Croston et al. 2005) . Thus, the L_X, gas temperature, absence of

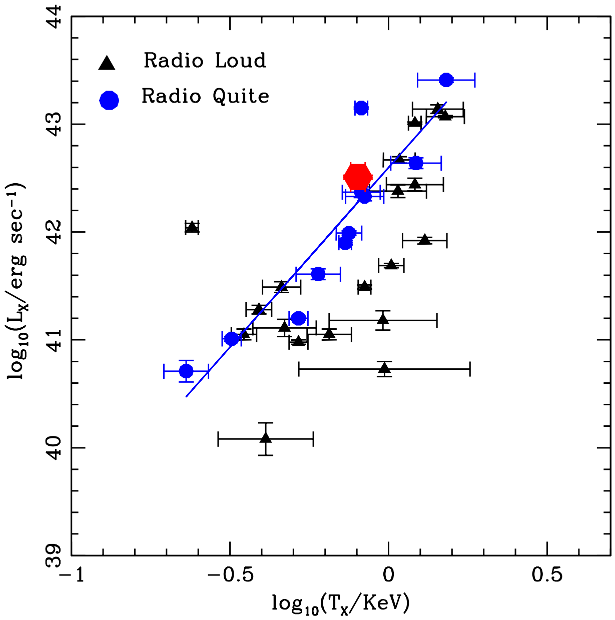

Figure 13. L_X plotted against the temperature of the hot gas for a sample of galaxies from Croston et al. (2005). The filled triangles represent radio-loud galaxies and the filled circles represent radio-quiet galaxies. CTD 86 is shown as the filled hexagon.

X-ray cavities, symmetric radio structures of CTD 86 all suggest that heating by the radio source in this system is not significant, probably due to the low power of the radio galaxy.

5.4 The radio & X-ray core emission

The origin of nuclear X-ray emission from FR I galaxies has not been understood clearly. The correlation observed between the X-ray and the radio emission suggests that the former has its origin in the jets. Figure 14 shows a plot of luminosity densities at 5 GHz and 1 keV for FR I galaxies taken from Evans et al. (2006) and CTD 86. From this figure it is clear that there is a large dispersion in the correlation. CTD 86 is close to the correlation line even though its X-ray luminosity is higher by an order of magnitude. Thus, based on this correlation, it is unlikely that the X-ray emission from FR I galaxies arises from the jets alone. X-ray emission from CTD 86 is also intrinsically absorbed by a large column within the host galaxy which is not likely if the entire X-ray emission were to arise from the jet. We have tested for the presence of an intrinsically unabsorbed X-ray power-law component that could arise from the jet. The contribution of such a power-law is at most 35% of the total X-ray emission in the $2 - 10$ keV band, therefore, most of the X-ray emission above 2 keV might be arising from the hot corona.

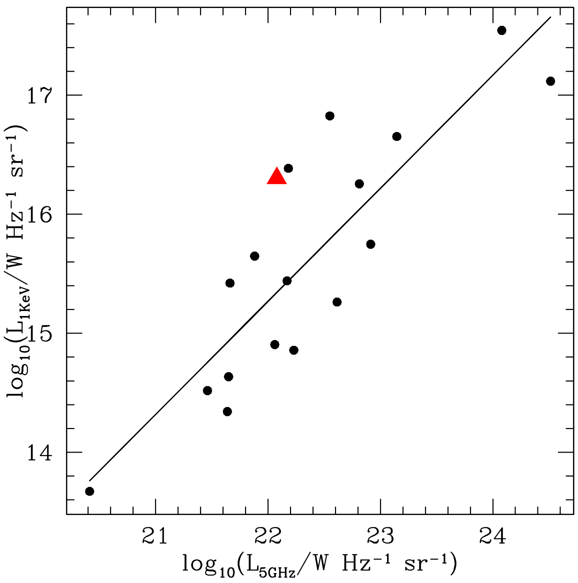

Figure 14. Relationship between the flux densities at 1 keV and 5 GHz for FR I galaxies. CTD 86 is shown as a triangle in this plot. All the data points except for CTD 86 were taken from Evans et al. (2006).

6 CONCLUSIONS

We have presented optical and X-ray imaging and spectroscopy of CTD 86 and its environment in both X-ray as well as Optical bands. The main results of the paper are as follows.

(i) Based on *ROSAT* HRI and *XMM-Newton* analysis, we have shown that X-ray emission from CTD 86 is extended (linear size $\sim$ 186 kpc). The spectral properties of the extended emission imply that the hot gas ($kT \sim 0.9$ keV, $n_e \sim 10^{-3}$ cm^{-3}, $M_{gas} = 1.83 \times 10^{11}\ M_{\odot}$ and Z=0.20 ± 0.02) surrounding the CTD 86 is similar to that found in galaxy groups.

(ii) There is no clear evidence for a strong interaction between the radio lobes and the hot gaseous environment of CTD 86.

(iii) Optical spectroscopy of nuclear region of CTD 86 has revealed the presence of only narrow emission lines, thus making it a narrow-line radio galaxy.

(iv) We found a clear evidence for the presence of a central X-ray core which is mildly active with a $2-10$ keV X-ray luminosity of 2.0×10^{42} ergs s^{-1}. Emission line properties of this mild AGN are similar to those of a type 2 AGN. The strengths of optical emission lines and X-ray luminosity suggest that CTD 86 hosts a low luminosity AGN.

(v) X-ray spectrum of the AGN in CTD 86 is absorbed by a large column, ($N_H = 5.9 \times 10^{22}$ cm^{-2}), which is among the highest observed from FR I galaxies. The amount of X-ray absorption and the large($i = 40 - 50\,$deg) inclination angle inferred from the radio-jets indicate that CTD 86 has a torus, similar to other type 2 AGN, and our line of sight passes through the outer region of the torus.

(vi) The large $L_X/L_{[O\ III]}$ ratio and very small relative accretion rate of CTD 86 suggest that the accretion disk of this low luminosity AGN is likely truncated at some large inner radius and the inner regions are filled with a hot flow.

(vii) We also report two bright X-ray sources, SDSS J142452.11+263715.1 and SDSS J142443.78+263616 near CTD 86. In the SDSS DR7 and DR8 data, SDSS J142452.11+263715.1 has been identified as a star and SDSS J142443.78+263616.2 as a galaxy. The optical spectrum of the first object, SDSS J142452.11+263715.1, shows broad emission lines and we classify this object as a quasar. The second object, SDSS J142443.78+263616.2, appears extended in the SDSS images and its strong X-ray emission suggests that may be a galaxy that probably hosts an AGN.

ACKNOWLEDGMENTS

MBP gratefully acknowledges support by DST INSPIRE scheme, New Delhi (sanction No. IF10179) and UGC, New Delhi through a research grant F.No. 36-240/2008(SR). This work is based on observations obtained with XMM-Newton, ESA science mission with instruments and contributions directly funded by ESA Member States and NASA. This research has made use of data from the High Energy Astrophysics Science Archive Research Center (HEASARC), provided by NASA's Goddard Space Flight Center.

REFERENCES

Arnaud, K. A., 1996, in Astronomical Society of the Pacific Conference Series, Vol. 101, Astronomical Data Analysis Software and Systems V, G. H. Jacoby & J. Barnes, ed., p. 17

Becker, R. H., White, R. L., & Helfand, D. J., 1994, in Astronomical Society of the Pacific Conference Series, Vol. 61, Astronomical Data Analysis Software and Systems III, Crabtree, D. R., Hanisch, R. J., & Barnes, J., eds., p. 165

Beers, T. C., Geller, M. J., Huchra, J. P., Latham, D. W., & Davis, R. J., 1984, ApJ, 283, 33

Bregman, J. N., Hogg, D. E., & Roberts, M. S., 1995, ApJ, 441, 561

Brough, S., Forbes, D. A., Kilborn, V. A., Couch, W., & Colless, M., 2006, MNRAS, 369, 1351

Canosa, C. M., Worrall, D. M., Hardcastle, M. J., & Birkinshaw, M., 1999, MNRAS, 310, 30

Cappellari, M. & Emsellem, E., 2004, PASP, 116, 138

Colla, G., Fanti, C., Fanti, R., Gioia, I., Lari, C., Lequeux, J., Lucas, R., & Ulrich, M. H., 1975, A&AS, 20, 1

Croston, J. H., Hardcastle, M. J., & Birkinshaw, M., 2005, MNRAS, 357, 279

Donato, D., Sambruna, R. M., & Gliozzi, M., 2004, ApJ, 617, 915

Evans, D. A., Worrall, D. M., Hardcastle, M. J., Kraft, R. P., & Birkinshaw, M., 2006, ApJ, 642, 96

Fanaroff, B. L. & Riley, J. M., 1974, MNRAS, 167, 31P

Fanti, R., Gioia, I., Lari, C., & Ulrich, M. H., 1978, A&AS, 34, 341

Georgantopoulos, I. & Georgakakis, A., 2005, MNRAS, 358, 131

Giovannini, G., Feretti, L., & Stanghellini, C., 1991, A&A, 252, 528

Giovannini, G., Taylor, G. B., Feretti, L., Cotton, W. D., Lara, L., & Venturi, T., 2005, ApJ, 618, 635

Grier, C. J., Mathur, S., Ghosh, H., & Ferrarese, L., 2011, ApJ, 731, 60

Gültekin, K., Richstone, D. O., Gebhardt, K., et al., 2009, ApJ, 698, 198

Hardcastle, M. J., 2005, Royal Society of London Philosophical Transactions Series A, 363, 2711

Helsdon, S. F. & Ponman, T. J., 2000, MNRAS, 315, 356

Ho, L. C., Filippenko, A. V., & Sargent, W. L. W., 1997, ApJS, 112, 315

Iyomoto, N., Makishima, K., Matsushita, K., Fukazawa, Y., Tashiro, M., & Ohashi, T., 1998, ApJ, 503, 168

Lakhchaura, K., Singh, K. P., Saikia, D. J., & Hunstead, R. W., 2011, ApJ, 743, 78

Maccacaro, T., Gioia, I. M., Wolter, A., Zamorani, G., & Stocke, J. T., 1988, ApJ, 326, 680

Mahdavi, A., Böhringer, H., Geller, M. J., & Ramella, M., 2000, ApJ, 534, 114

Mahdavi, A. & Geller, M. J., 2001, ApJ, 554, L129

Mathews, W. G. & Brighenti, F., 2003, ARA&A, 41, 191

McNamara, B. R. & Nulsen, P. E. J., 2007, ARA&A, 45, 117

Merkelijn, J. K., 1968, Australian Journal of Physics, 21, 903

Mulchaey, J. S., 2000, ARA&A, 38, 289

Ortiz-Gil, A., Guzzo, L., Schuecker, P., Böhringer, H., & Collins, C. A., 2004, MNRAS, 348, 325

O'Sullivan, E., Forbes, D. A., & Ponman, T. J., 2001, MNRAS, 328, 461

O'Sullivan, E., Ponman, T. J., & Collins, R. S., 2003, MNRAS, 340, 1375

Paolillo, M., Fabbiano, G., Peres, G., & Kim, D.-W., 2003, ApJ, 586, 850

Parma, P., Fanti, C., Fanti, R., Morganti, R., & de Ruiter, H. R., 1987, A&A, 181, 244

Parma, P., Murgia, M., Morganti, R., Capetti, A., de Ruiter, H. R., & Fanti, R., 1999, A&A, 344, 7

Pfeffermann, E., Briel, U. G., Hippmann, H., et al., 1987, in Society of Photo-Optical Instrumentation Engineers (SPIE) Conference Series, Vol. 733, Society of Photo-Optical Instrumentation Engineers (SPIE) Conference Series, E.-E. Koch & G. Schmahl, ed., p. 519

Plionis, M. & Tovmassian, H. M., 2004, A&A, 416, 441

Sarazin, C. L., 1986, Reviews of Modern Physics, 58, 1

Snowden, S. L., Mushotzky, R. F., Kuntz, K. D., & Davis, D. S., 2008, A&A, 478, 615

Spinrad, H., Marr, J., Aguilar, L., & Djorgovski, S., 1985, PASP, 97, 932

Strüder, L., Briel, U., Dennerl, K., et al., 2001, A&A, 365, L18

Truemper, J., 1982, Advances in Space Research, 2, 241

Turner, M. J. L., Abbey, A., Arnaud, M., et al., 2001, A&A, 365, L27

Vasudevan, R. V. & Fabian, A. C., 2007, MNRAS, 381, 1235

Xue, Y.-J. & Wu, X.-P., 2000, ApJ, 538, 65